Verification of a simple model for the lateral-load analysis and design of unbonded post-tensioned precast concrete walls

Felipe J. Perez and Omar Mauricio

- This paper presents the results of a parametric study conducted using a fiber model and simple model, which were developed in previous research, to investigate the adequacy of the simple model for a broader range of parameters.
- Results show that the simple model accurately represents the lateral-load response, characterized by base shear and roof drift values at specific limit states obtained using the fiber model.
- The simple model and the fiber model show similar values of base shear and roof-drift response, and they show similar trends for each parameter variation.

Buildings with reinforced concrete walls as the primary lateral-load-resisting system have demonstrated superior seismic performance in past earthquakes.[1] Precast concrete construction offers many benefits over cast-in-place concrete, including improved quality control, fast erection, cost effectiveness, and construction efficiencies. Using precast concrete structural walls for earthquake resistance combines the benefits of precast concrete construction and lateral-load-resisting walls.

Several precast concrete seismic structural systems were developed under the PRESSS (Precast Seismic Structural Systems) program. PRESSS research showed that using unbonded post-tensioning to connect precast concrete subassemblages results in beneficial hysteretic behavior characterized by a nonlinear elastic load-deformation response.[2–4] The nonlinearity results from gaps opening along the joints as the precompression due to prestressing is overcome by the moment due to lateral loads. This early work showed that by using unbonded post-tensioning, it is possible to prevent or delay yielding in the post-tensioning steel and thus preserve the prestress during seismic response. Perez et al.[5,6] experimentally investigated the lateral-load response of large-scale unbonded post-tensioned precast concrete walls and showed that they have excellent self-centering capabilities before failure. These types of unbonded post-tensioned walls are broadly classified as a jointed construction seismic system, as opposed to an emulative construction seismic system, which is designed to perform comparable to an equivalent cast-in-place reinforced concrete system.[7] Other types of

unbonded post-tensioned walls include hybrid unbonded post-tensioned precast concrete walls and unbonded post-tensioned precast concrete walls with energy dissipaters (that is, dampers) that use either longitudinal mild steel reinforcement between the base joint and the foundation or supplemental dampers for inelastic energy dissipation.[8,9,10,11]

Several analytical models have been proposed to estimate the nonlinear behavior of unbonded post-tensioned precast concrete walls subjected to combined gravity and lateral loads. One model, referred to as the fiber model in this paper, was proposed by Kurama et al.[12,13] and uses a nonlinear fiber element in a finite element program to estimate the response of unbonded post-tensioned precast concrete walls.[14] A second model, referred to as the simple model in this paper, was proposed by Perez et al.[15] and consists of several closed-form expressions that generate a trilinear idealization of the base shear versus roof drift behavior of unbonded post-tensioned precast concrete walls. Both models consider several critical limit states in the lateral-load response of these walls. The fiber model and simple model were previously validated with limited available experimental results.[6,15] A parametric study was previously conducted by Kurama et al.[12,13] using the fiber model to investigate the response of unbonded post-tensioned precast concrete walls under combined gravity and lateral loads.

This paper investigates the accuracy of the simple model by conducting a similar parametric study and comparing the simple model results with those of the fiber model. Because the simple model was verified using only five selected experiments, a more complete verification of the simple model including multiple parameter variations is made available through this study.[5,6] In the absence of experimental data, the simple model was verified using concurrent analysis results from the fiber model proposed by Kurama et al.[12,13] The simple model used in the present study does not apply to hybrid walls but can be modified to do so. Smith et al.[10] propose a linear-elastic effective stiffness model to evaluate the roof drift of hybrid walls, but it is only applicable prior to significant nonlinear behavior of the concrete at the wall toes and significant yielding of the energy-dissipating reinforcement crossing the base joint. Palermo et al.[11] derived an approximate closed-form section-equilibrium solution at ultimate conditions for rectangular sections with lumped mild steel reinforcement, which may be used to extend the simple model used in the present study to include the effects of bonded mild reinforcement across the base joint.

Background

This section gives background information on unbonded post-tensioned precast concrete walls. First, the general configuration of the wall considered in this study is presented. Next, key limit states that characterize the lateral load behavior of unbonded post-tensioned precast concrete walls are identified. This is followed by a brief introduction of two analytical models used to obtain the lateral-load behavior of unbonded post-tensioned precast concrete walls: the simple model and the fiber model. Last, the parameters of the proto-

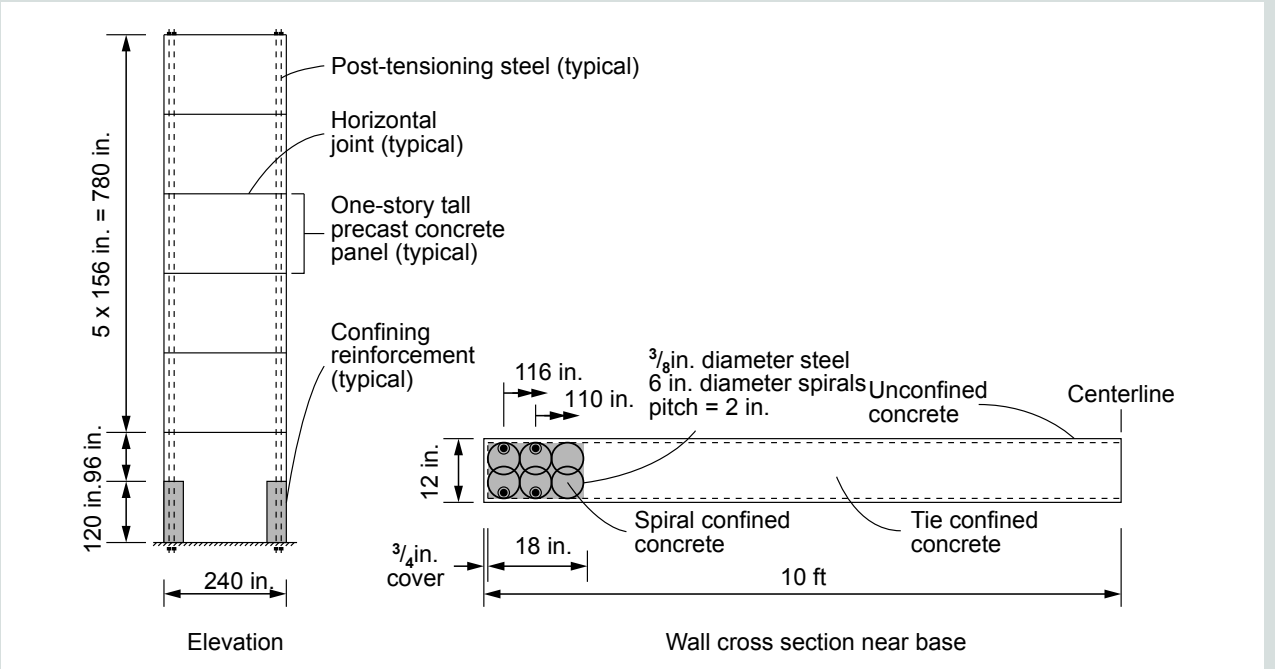

Figure 1. Unbonded post-tensioned precast concrete wall.
Source: Adapted from Kurama et al. (1996).
Note: 1 in. = 25.4 mm; 1 ft = 0.305 m.

type wall considered in this study are summarized.

Unbonded post-tensioned precast concrete wall

Figure 1 shows a diagram of the unbonded post-tensioned precast concrete wall that was considered in this study. The wall consisted of six one-story precast concrete panels that were stacked vertically and connected along horizontal joints using post-tensioning steel that ran vertically through ducts in the panels. The post-tensioning steel was anchored within the foundation, pulled to a desired level of tension, and secured at the roof. The ducts containing the post-tensioning steel remained ungrouted, resulting in unbonded behavior. The wall had special confining reinforcement at the ends of the base panel so that it could sustain the large compressive strains that developed under combined vertical and lateral loads. The confining reinforcement consisted of interlocking spirals (Fig. 1), but it can also consist of special confining ties and supplemental reinforcement as recommended by Perez et al.[5] to mitigate the possibility of an unstable buckling failure in the base panel. In the present study, the post-tensioning steel was located inside the confined concrete regions of the wall, instead of closer to the center of the wall, as previously considered by Perez et al.[5,6] As a result, the present study validates the simple model for conditions that are different than in previous work.

Perez et al.[5,6] experimentally evaluated the lateral-load response of five large-scale unbonded post-tensioned precast concrete walls and compared the experimental results with those from the simple model and the fiber model. **Figure 2** compares the base shear V versus roof drift Θ response for a wall tested monotonically to failure with results from the simple model and fiber model. The roof drift was computed by dividing the lateral displacement at the roof by the wall height. The experimental curve has repeated reductions in base shear, which occurred when the test was paused and the gravity load jack in the test fixture was adjusted. The experimental results are in agreement with results obtained using both the simple model and the fiber model. Furthermore, these analytical models captured several key limit states that characterize the lateral-load response of the wall, as described in the following section. The analytical models used in the present study were based on walls with ductile post-tensioning systems capable of developing large tensile strains beyond first yield, such that the wall roof drift at tensile fracture of post-tensioning steel exceeds the roof drift corresponding to confinement failure of the walls. Furthermore, the analytical models assume that sufficient confinement reinforcement is provided at the wall toes, and that the total area of post-tensioning steel is sufficiently limited so that confinement failure does not occur prematurely (that is, before post-tensioning steel yields).

Key limit states

The lateral-load response of an unbonded post-tensioned precast concrete wall is characterized by the following key limit states: decompression at the wall base, effective linear limit of response, initiation of cover spalling, yielding of the post-tensioning steel, and crushing of confined concrete (Fig. 2). These limit states are described in greater detail by Kurama et al.[12,13,16] and Perez et al.,[15] but a brief description is provided herein. Decompression occurs at the base of the wall when precompression due to prestress and gravity loads is overcome by the application of lateral loads. Softening, or a substantial

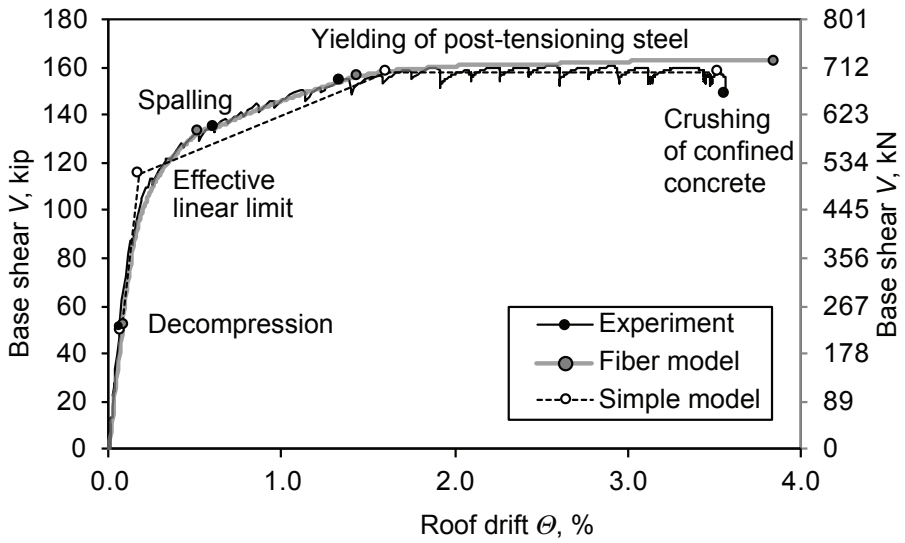

Figure 2. Comparison of experimental and analytical results for an unbonded post-tensioned precast concrete wall under monotonic loading.
Sources: Perez et al. (2004) and Perez et al. (2013).

loss of lateral stiffness, in an unbonded post-tensioned precast concrete wall occurs from gap-opening behavior along the horizontal joint at the base and from nonlinear behavior in the concrete in compression.[12,13] The point at which softening is apparent is referred to as the effective linear limit. The initiation of cover spalling occurs when the unconfined concrete at the toe of the wall spalls. The spalling limit state is not considered by the simple model because it represents a serviceability limit state and does not appreciably affect overall seismic response. Yielding of the post-tensioning steel refers to the first occurrence of tension yielding in the post-tensioning bars located the farthest from the wall centerline. Last, crushing of confined concrete refers to a concrete confinement failure at the wall base. The wall loses all lateral resistance upon reaching the crushing of confined concrete limit state.

Simple model

The simple model is based on trilinear idealized base shear versus roof drift behavior (Fig. 2) and uses "simple" formulas to estimate the base shear and roof drift at the points of effective linear limit, yielding of post-tensioning steel, and crushing of confined concrete, which define the idealization. The simple model applies to a generalized unbonded post-tensioned precast concrete wall comprising r one-story wall panels, three groups of post-tensioning steel with different initial prestress forces, and eccentric gravity loads with magnitudes and eccentricities that vary along the height of the wall. **Figure 3** shows the following forces acting on a generalized unbonded post-tensioned precast concrete wall:

- $F_{w,i}$, which is a lateral force on wall at floor i
- a wall base shear force V_w that is in equilibrium with the lateral loads
- a gravity load at ith floor level, including load supported by the wall and wall self-weight N_i acting at an eccentricity $e_{N,i}$

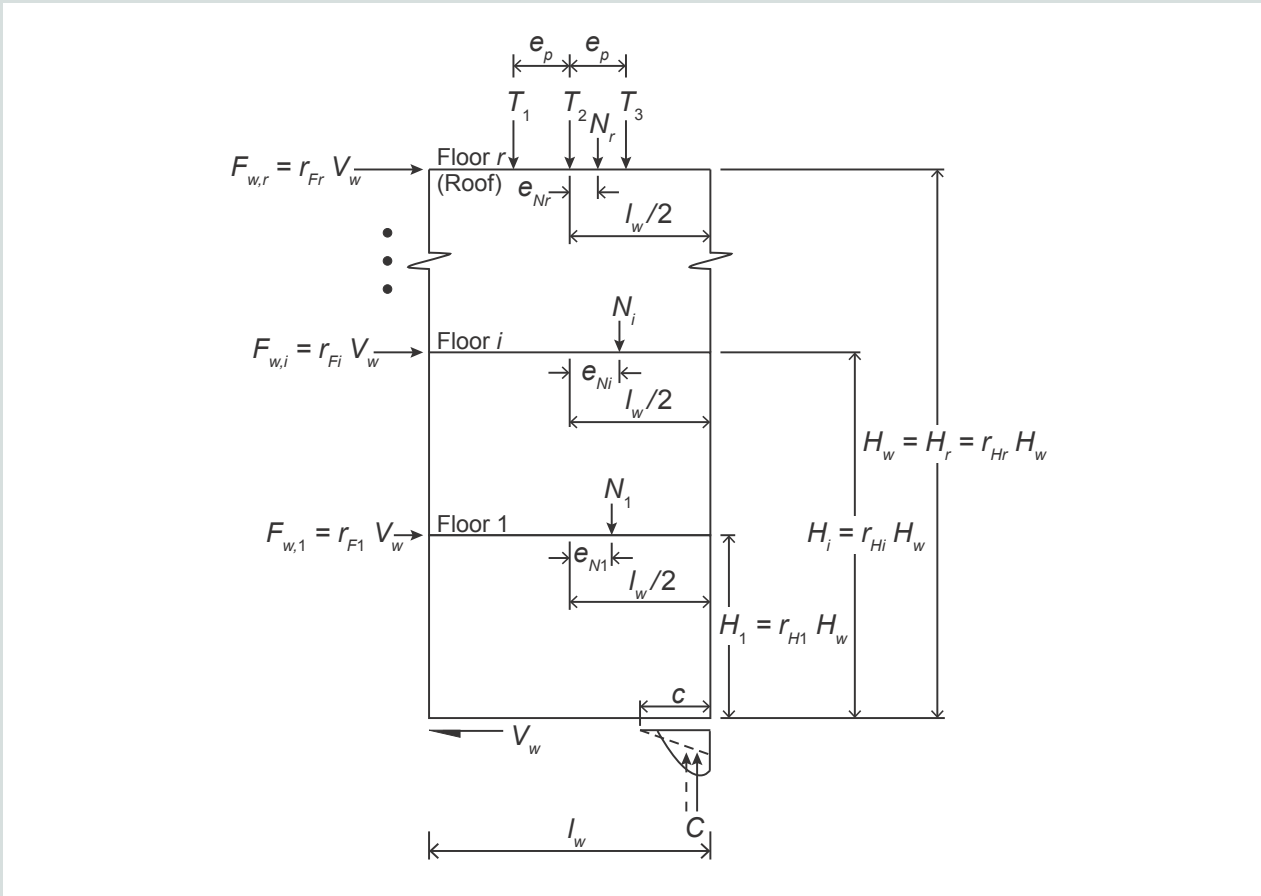

Figure 3. Forces on an unbonded post-tensioned precast concrete wall. Note: c = contact length at wall base; C = concrete compression stress resultant at wall base; e_{Ni} = eccentricity of N_i measured from the wall centerline; e_{Nr} = eccentricity of N_r measured from the wall centerline; e_p = eccentricity of post-tensioning steel from wall centerline to centroid of post-tensioning steel group; $F_{w,i}$ = lateral force on wall at floor i; $F_{w,r}$ = lateral force on wall at roof level; H_i = height of floor level i measured from the base of the wall; H_r = height of roof level measured from the base of the wall = H_w; H_w = total wall height; l_w = wall length; N_i = gravity load at ith floor level, including panel self-weight; N_r = gravity load at roof level, excluding top panel self-weight; r = total number of stories in a wall; r_{Fi} = ratio of the force in the ith floor level to the wall base shear; r_{Fr} = ratio of the force at the roof level to the wall base shear; r_{Hi} = ratio of the ith floor height to the total height of the wall; r_{Hr} = ratio of the roof height to the total height of the wall (equal to unity); T_1 = total force in post-tensioning steel group 1; T_2 = total force in post-tensioning steel group 2; T_3 = total force in post-tensioning steel group 3; V_w = wall base shear (equal to sum of applied lateral loads).

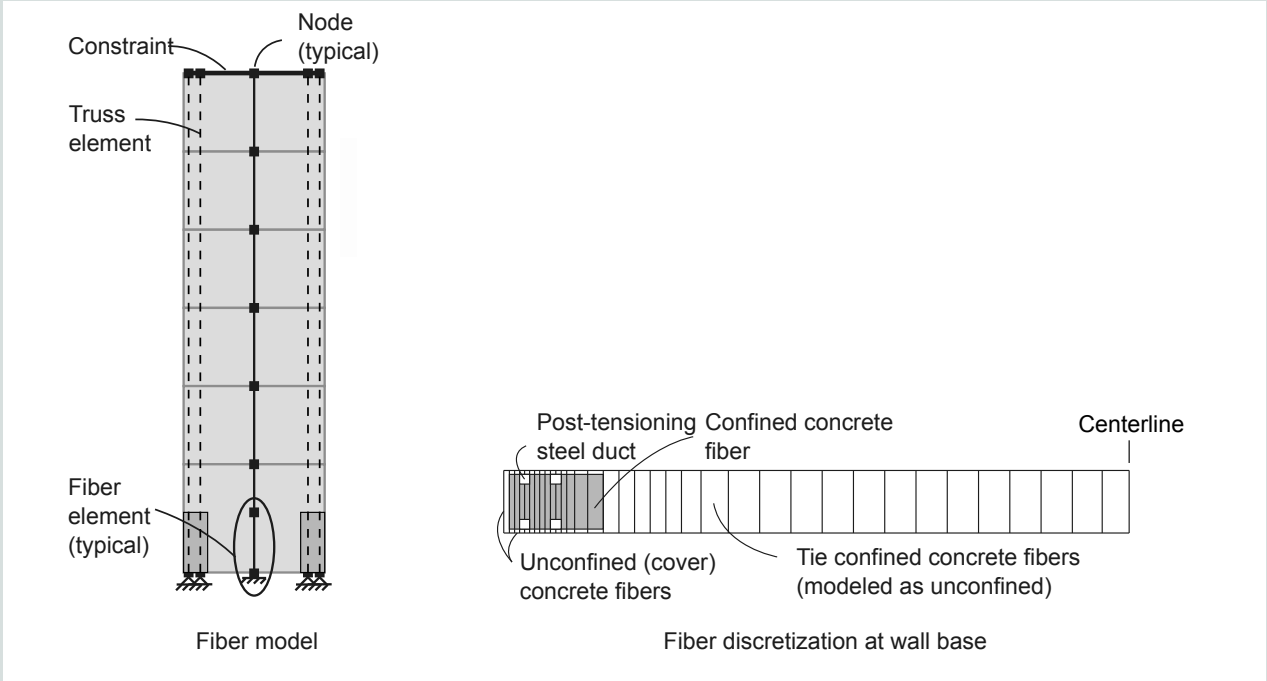

Figure 4. Fiber model of an unbonded post-tensioned precast concrete wall.

- post-tensioning forces in three groups of post-tensioning steel T_1, T_2, and T_3
- a concrete compression stress resultant at the wall base C

The wall length, height, and contact length at the base are denoted as l_w, H_w, and c, respectively. The lateral load at each floor level is expressed as a fraction of the total base shear using the parameters r_{F1}, r_{Fi}, and r_{Fr} for floor 1, floor i, and the roof, respectively. Similarly, the height of each floor relative to the base is expressed as a fraction of the total wall height using the parameters r_{H1}, r_{Hi}, and r_{Hr} for floor 1, floor i, and the roof, respectively. The wall forces in Fig. 3 were used in the derivations of the base shear and roof drift response quantities for the simple model. Perez et al.[6] provide a detailed development of the simple model and the related formulas and present a performance-based seismic design methodology for unbonded post-tensioned precast concrete walls that uses the simple model to estimate their capacities. Perez et al.[15] present the simple model formulas in an abridged form; thus, the formulas are not reproduced herein. The unbonded post-tensioned precast concrete wall (Fig. 1) has four post-tensioning bars at two different eccentricities. The simple model considers only one eccentric post-tensioning group on either side of the wall centerline. Thus, the four post-tensioning bars in Fig. 1 are considered to make up post-tensioning steel group 1 in the simple model (post-tensioning steel group 3 is on the opposite end of the wall). Similarly, the unbonded post-tensioned precast concrete wall in Fig. 1 does not have a concentric group of post-tensioning steel. Thus, post-tensioning steel group 2 in the simple model is neglected.

Fiber model

The fiber model developed by Kurama et al.[13] uses fiber beam–column elements to model the precast concrete wall panels and nonlinear truss elements to model the post-tensioning steel. **Figure 4** is a schematic of a fiber model for the unbonded post-tensioned precast concrete wall depicted in Fig. 1. The wall was modeled using seven fiber beam–column elements (Fig. 4). A total of 98 fibers were used to discretize the cross section of the wall near the base (Fig. 4). Multilinear uniaxial stress-strain relationships were used to model the unconfined concrete and spiral-confined concrete. An unconfined concrete compressive strength f_c' of 6 ksi (41.4 MPa) and a confined concrete compressive strength f_{cc}' of 11.5 ksi (79.3 MPa) were specified. The uniaxial stress-strain relationship used to model the spiral-confined concrete was based on the confinement model proposed by Mander et al.[17] The confining effect of ties in the wall panels are so small that they can be neglected.[13] Thus, the tie-confined concrete regions of the wall were modeled using unconfined concrete properties. Modeling of gap-opening behavior at the wall base in the fiber model is discussed by Kurama et al.[13] Gap-opening displacement along a horizontal joint was represented as distributed tensile deformation between panels (and between the base panel and the foundation). For gap-opening displacements to be distributed in the wall panels, the tensile strength of the concrete fibers was neglected.

The post-tensioning steel was modeled using a bilinear stress-strain relationship with an elastic modulus E_p of 29,000 ksi (200 GPa), a yield stress f_{py} of 145 ksi (1000 MPa), an ultimate tensile strength f_{pu} of 160 ksi (1100 MPa), and a

Table 1. Properties of the prototype unbonded post-tensioned precast concrete wall PW1

Wall parameters	Wall length l_w, in.	240
	Wall height H_w, in.	996
	Wall thickness t_w, in.	12
	Confined length l_{cr}, in.	18
	Confined height h_{cr}, in.	120
	Confined thickness t''_w, in.	9.375
	Critical crushing height $H_{cr} = 2t''_w$, in.	18.75
	Stories r	6
	First-floor height ratio r_{H1}	0.217
	Second-floor height ratio r_{H2}	0.373
	Third-floor height ratio r_{H3}	0.530
	Fourth-floor height ratio r_{H4}	0.687
	Fifth-floor height ratio r_{H5}	0.843
	Roof-level height ratio r_{Hr}	1.0
	Net cross-sectional area $A_{w,net}$, in.^{2}	2841
	Moment of inertia of the uncracked section I_w, in.^{4}	1.333×10^7
	Effective shear area A'_w, in.^{2}	2367
Prestress parameters	Total area of post-tensioning steel in the wall $A_p = A_{p1} + A_{p2} + A_{p3}$, in.^{2}	(4 + 0 + 4) = 8
	Eccentricity of post-tensioning steel from wall centerline to centroid of post-tensioning steel group e_p, in.	113
	Modulus of elasticity of post-tensioning steel E_p, ksi	29,000
	Yield stress of post-tensioning steel f_{py}, ksi	145
	Tensile strength of post-tensioning steel f_{pu}, ksi	160
	Initial stress in post-tensioning steel in group 1 f_{p1i} = initial stress in post-tensioning steel in group 3 $f_{p3i} = 0.57\ f_{pu}$, ksi	92.1
	Initial stress in post-tensioning steel in group 2 f_{p2i}, ksi	0
	Total initial prestress force in post-tensioning steel group 1 T_{1i} = total initial prestress force in post-tensioning steel group 3 T_{3i}, kip	368.5
	Total initial prestress force in post-tensioning steel group 2 T_{2i}, kip	0
	Average initial stress in concrete due to prestressing $f_{ci,P} = (T_{1i} + T_{2i} + T_{3i})/A_{w,net}$, ksi	0.259
Concrete properties	Unconfined concrete compressive strength f'_c, ksi	6
	Elastic modulus of concrete E_c, ksi	4415
	Shear modulus of concrete G_c, ksi	1920
	Volumetric ratio of spiral reinforcement ρ_{sp}, %	3.67
	Confined concrete compressive strength f'_{cc}, ksi	11.5
	Ultimate strain capacity of confined concrete ε_{cu}, in./in.	0.0364
Load parameters	Total gravity load at the wall base $N = \sum_{i=1}^{r} N_i$, kip	1278
	Eccentricity of gravity load at ith floor level N_i measured from the wall centerline e_{Ni} (for i = 1 to r)	0
	First-floor load ratio r_{F1}	0.0472
	Second-floor load ratio r_{F2}	0.0906
	Third-floor load ratio r_{F3}	0.1379
	Fourth-floor load ratio r_{F4}	0.1882
	Fifth-floor load ratio r_{F5}	0.2408
	Roof-level load ratio r_{Fr}	0.2954

Source: Data from Kurama et al. (1996).

Note: A_{p1} = total area of post-tensioning steel in post-tensioning steel group 1; A_{p2} = total area of post-tensioning steel in post-tensioning steel group 2; A_{p3} = total area of post-tensioning steel in post-tensioning steel group 3. 1 kip = 4.45 kN; 1 in. = 25.4 mm; 1 ksi = 6.895 MPa.

postyield tangent modulus of 429 ksi (2960 MPa). One truss element was used to model a pair of post-tensioning bars with the same eccentricity.

Prototype wall parameters

Figure 1 shows the prototype unbonded post-tensioned precast concrete wall considered in this study. All parameters given in **Table 1** use notation consistent with the simple model described earlier. The following prestress parameters were taken as zero: area of post-tensioning steel group 2 A_{p2}, initial stress in post-tensioning steel group 2 f_{p2i}, and total initial prestress force in post-tensioning steel group 2 T_{2i}. These parameters correspond to a concentric post-tensioning steel group, in accordance with the simple model derivations (prestress force T_2 in Fig. 3). Because the walls considered in the present study did not have a concentric post-tensioning steel group, these parameters were neglected. The load parameter N represents the total gravity load at the wall base. Because the gravity loads were concentric along the wall height, the eccentricity of the gravity load at each floor level e_{Ni} was set equal to zero.

Parametric study

This section presents an analytical parametric study of unbonded post-tensioned precast concrete walls under monotonic pseudostatic lateral loads. The results of the parametric study were obtained using the fiber model and the simple model described previously. These comparisons were the basis for validating the simple model.

The study considered a total of 16 different walls: the prototype wall and 15 other walls that include variations of the properties of the prototype wall. The prototype wall is referred to as PW1, and the remaining walls are referred to as W2 through W16.

Structural design parameters

The effect of four structural design parameters on the monotonic nonlinear lateral load behavior of the prototype wall was investigated. The four design parameters were: total area of post-tensioning steel in the wall A_p, initial stress in the post-tensioning steel after the application of prestress forces and gravity loads on the wall f_{pi} with constant A_p to produce a variable total initial prestress force on the wall P_i equal to $A_p f_{pi}$, initial stress in post-tensioning steel f_{pi} with variable A_p to produce a constant P_i, and initial stress in concrete due to varying gravity loads $f_{ci,N}$ with constant initial stress in concrete due to prestressing $f_{ci,P}$. **Table 2** summarizes the structural design pa-

Table 2. Summary of structural design parameters varied in current study

Parameter investigation	Wall	A_p, in.^{2}	f_{pi}, ksi	P_i, kip	N, kip	$f_{ci,P}$, ksi	$f_{ci,N}$, ksi	f_{ci}, ksi
Prototype	PW1	8.0	92	736	1278	0.259	0.450	0.709
Variable A_p	W2	4.0	92	368	1278	0.130	0.450	0.579
	W3	6.0	92	552	1278	0.194	0.450	0.644
	W4	10.0	92	920	1278	0.324	0.450	0.774
	W5	12.0	92	1104	1278	0.389	0.450	0.838
Variable f_{pi}	W6	8.0	65	520	1278	0.183	0.450	0.633
	W7	8.0	80	640	1278	0.225	0.450	0.675
	W8	8.0	108	864	1278	0.304	0.450	0.754
	W9	8.0	120	960	1278	0.338	0.450	0.788
Variable A_p, variable f_{pi}, constant P_i	W10	6.0	123	736	1278	0.259	0.450	0.709
	W11	7.0	105.1	736	1278	0.259	0.450	0.709
	W12	10.0	73.6	736	1278	0.259	0.450	0.709
	W13	12.0	61.3	736	1278	0.259	0.450	0.709
Variable $f_{ci,N}$, constant $f_{ci,P}$	W14	8.0	92.0	736	426	0.259	0.150	0.409
	W15	8.0	92.0	736	639	0.259	0.225	0.484
	W16	8.0	92.0	736	852	0.259	0.300	0.559

Note: A_p = total area of post-tensioning steel in the wall; f_{ci} = initial stress in concrete due to post-tensioning and gravity loads; $f_{ci,N}$ = initial stress in concrete due to gravity loads; $f_{ci,P}$ = average initial stress in concrete due to prestressing; f_{pi} = stress in post-tensioning steel after the application of prestress forces and gravity loads; N = total gravity load at the wall base; P_i = total force in the post-tensioning steel after the application of prestress forces and gravity loads. 1 in.^{2} = 645.2 mm^2; 1 kip = 4.448 kN; 1 ksi = 6.895 MPa.

rameters that were varied for all of the walls considered in this study. Parameters not shown in Table 2 remained unchanged from those given in Table 1 for wall PW1.

Area of post-tensioning steel

The objective of this parameter investigation was to verify that the simple model can adequately capture the effect of varying the total area of post-tensioning steel in the wall A_p. Varying A_p while keeping the initial stress in the post-tensioning steel f_{pi} constant varies the initial stress in the wall due to post-tensioning and gravity loads f_{ci}. Five walls were considered in this parameter investigation (PW1 and W2 to W5).

Initial stress in post-tensioning steel with constant A_p

The objective of this parameter investigation was to verify that the simple model adequately captures the effect of varying the initial stress in the post-tensioning steel f_{pi} while keeping the total area of post-tensioning steel in the wall A_p constant. Varying f_{pi} while keeping A_p constant varies the initial stress in the wall due to post-tensioning and gravity loads f_{ci}. Five walls were considered in this parameter investigation (PW1 and W6 to W9).

Initial stress in post-tensioning steel with variable A_p and constant P_i

The objective of this parameter investigation was to verify that the simple model adequately captures the effect of varying both the initial stress in the post-tensioning steel f_{pi} and the total area of post-tensioning steel in the wall A_p such that the total initial prestress force on the wall after the application of prestress forces and gravity loads P_i equal to $f_{pi}A_p$ remains constant. Furthermore, the choice of f_{pi} and A_p values produces a constant initial stress in the wall due to prestressing, $f_{ci,P}$ equal to $P_i/A_{w,net}$, where $A_{w,net}$ is the net cross-sectional area of the wall. Five walls were considered in this parametric investigation (PW1 and W10 to W13).

Initial stress in concrete due to varying gravity loads

The objective of this parametric investigation was to verify that the simple model adequately captures the effect of varying the initial stress in concrete due to varying gravity loads $f_{ci,N}$ while keeping the initial stress in the wall due to prestressing $f_{ci,P}$ constant. This parametric investigation was achieved by varying the amount of total gravity load sustained by the wall N. Four walls were considered in this parameter investigation (PW1 and W14 to W16).

Analysis response quantities

The main response quantities from the analyses focus on base shear V and roof drift Θ values corresponding to four key limit states: decompression (V_{dec} and Θ_{dec}), effective linear limit (V_{ell} and Θ_{ell}), yielding of post-tensioning steel (V_{llp} and Θ_{llp}), and crushing of confined concrete (V_{ccc} and Θ_{ccc}). The limit state corresponding to cover spalling was not considered in this study because this limit state is not considered by the simple model.

The analysis response quantities are presented using base-shear-roof-drift plots. In addition, plots were generated to compare the sensitivity of a given parameter (for example, f_{pi}) on the base shear and roof drift quantities for both the simple model and fiber model. The results of the simple model were compared with those of the fiber model to validate the simple model.

Results and discussion

This section presents the results of the parametric study. First, the observed lateral-load behavior of the prototype wall is presented. Next, the plots used to present the results of the parametric study are explained. Finally, the effects of four structural design parameters on the analysis response quantities are discussed.

Prototype wall behavior

Figure 5 shows the base-shear-roof-drift response of the prototype wall (PW1) obtained from the simple model and the fiber model. The figure shows the occurrence of the key limit states considered by both models. **Table 3** summarizes the base shear and roof drift corresponding to the key limit states for both the simple model and fiber model. All base shear response quantities estimated by the simple model are within 4% of the base shear response quantities obtained using the

Table 3. Base shear V and roof drift response Θ for wall PW1 using simple model and fiber model

Wall ID	Model	Decompression at the wall base		Effective linear limit		Yielding of post-tensioning steel		Crushing of confined concrete	
		Θ_{dec}, %	V_{dec}, kip	Θ_{ell}, %	V_{ell}, kip	Θ_{llp}, %	V_{llp}, kip	Θ_{ccc}, %	V_{ccc}, kip
PW1	Simple model	0.041	108.6	0.104	271.5	0.985	354.2	3.08	354.2
	Fiber model	0.041	112.8	0.213	282.0	0.908	360.8	3.09	365.0

Note: 1 kip = 4.448 kN.

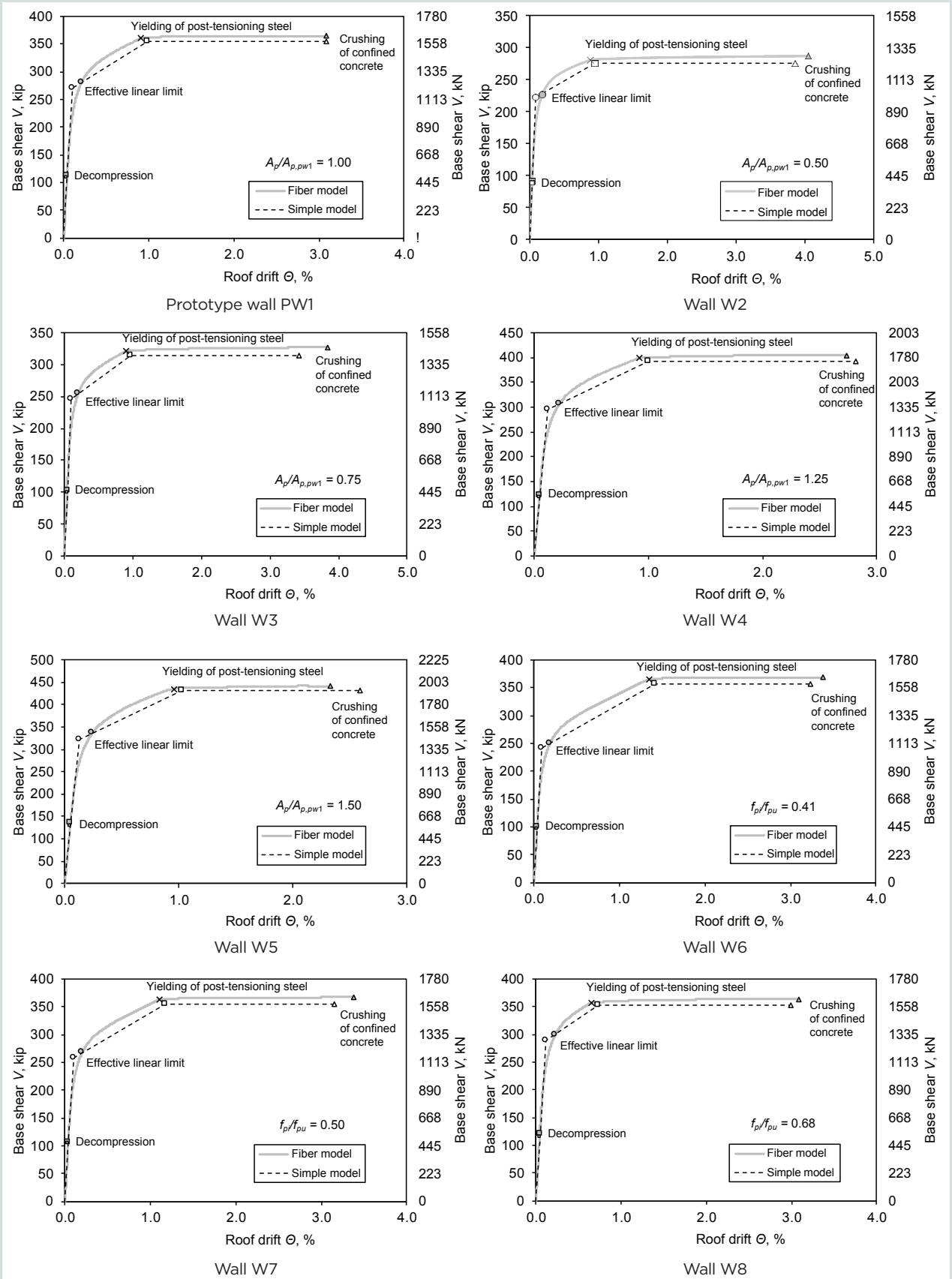

Figure 5. Base-shear-roof-drift response of prototype wall PW1 to wall W16. Note: A_p = total area of post-tensioning steel in the wall; $A_{p,pw1}$ = total area of post-tensioning steel in the prototype wall PW1; f_{pi} = stress in post-tensioning steel after the application of prestress forces and gravity loads; f_{pu} = ultimate tensile strength of post-tensioning steel. (*Continued on p. 60.*)

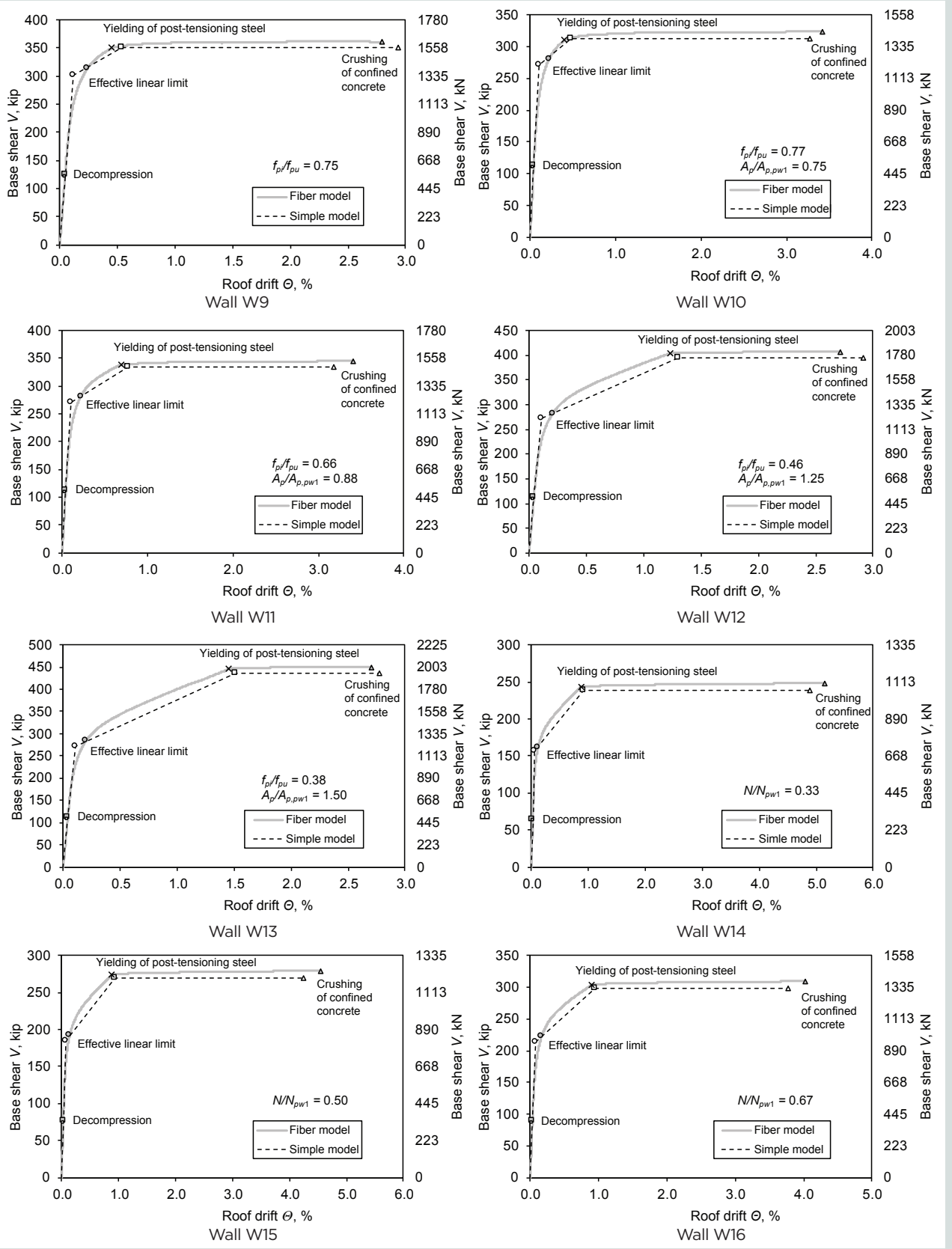

Figure 5. (*Continued from p. 59.*) Base-shear-roof-drift response of prototype wall PW1 to wall W16. Note: A_p = total area of post-tensioning steel in the wall; $A_{p,pw1}$ = total area of post-tensioning steel in the prototype wall PW1; f_{pi} = stress in post-tensioning steel after the application of prestress forces and gravity loads; f_{pu} = ultimate tensile strength of post-tensioning steel; N = total gravity load at the wall base; N_{pw1} = total gravity load at the base of prototype wall PW1.

fiber model. The roof drift at decompression Θ_{dec} and at crushing of confined concrete Θ_{ccc} are in excellent agreement. The roof drift at yielding of the post-tensioning steel Θ_{llp} was slightly overestimated by the simple model. This is because the simple model treats the four post-tensioning bars located at the end of the wall (Fig. 1) as one group of bars located at the centroid of the four bars. Because the centroid of the group of bars was slightly closer to the middle of the wall, the onset of yielding was delayed, resulting in a slightly larger roof drift. This was true of all walls considered in this study.

The largest discrepancy between the two models occurred with the roof drift at the effective linear limit state Θ_{ell}. Because softening in an unbonded post-tensioned precast concrete wall occurs in a smooth and continuous manner, there is no specific stress condition associated with the effective linear limit state. Thus, Θ_{ell} is estimated for the fiber model by first computing the base shear at the effective linear limit as V_{ell} equals $2.5V_{dec}$, per Kurama et al.,[12] then locating the corresponding roof drift on the base-shear-roof-drift response curve. The simple model requires the evaluation of V_{ell} first, then Θ_{ell} is computed from a linear elastic analysis. Thus, Θ_{ell} based on the simple model does not lie directly on the base-shear-roof-drift response curve obtained using the fiber model. As a result, a large discrepancy is observed when comparing the specific values of Θ_{ell} based on the simple model and fiber model. However, the simple model adequately captures the effective linear limit state in the trilinear idealization (Fig. 5).

Results of the parametric study

Results of the parametric study using the simple model and fiber model are presented in two ways: base-shear-roof-drift plots for each wall considered in the parameter investigation and plots of relationships between the analysis response quantities and the design parameters.

Base-shear-roof-drift plots

Figures 5 shows the base-shear-roof-drift response curves obtained using the simple model and fiber model for each of the walls considered in the parameter investigation. The roof drift, in percent, was obtained by normalizing the roof displacement with respect to the height of the wall H_w, which was 83 ft (25 m). In each figure, the parameter being investigated was normalized with respect to the same parameter for the prototype wall PW1. The trilinear idealized response obtained using the simple model was plotted for each wall to determine the accuracy of the simple model.

Analysis response quantities versus design parameters

Figures 6 through **9** show the relationships between the structural design parameters and the analysis response quantities. Each figure shows the effect of one design parameter on the normalized base shear and roof drift response quantities obtained using the simple model and the fiber model. The base shear response quantities were normalized with respect to the base shear at the limit state corresponding to yielding of post-tensioning steel for PW1, calculated using the fiber model V_{llp} of 360.8 kip (1605 kN). In Fig. 6, the area of post-tensioning steel was normalized with respect to the area of post-tensioning steel of PW1 $A_{p,pw1}$ of 8.0 in.^{2} (5200 mm^2). In Fig. 7 and 8, the initial prestress in the post-tensioning steel f_{pi} was normalized with respect to the ultimate strength of the post-tensioning steel f_{pu} of 160 ksi (1100 MPa). In Fig. 9, the total gravity load N was normalized with respect to the total gravity load supported by PW1 N_{pw1} of 1278 kip (5685 kN).

Discussion of parametric study results

The accuracy of the simple model (that is, the trilinear idealized lateral load behavior of unbonded post-tensioned precast concrete walls obtained using the simple model) is examined first, followed by a discussion of the effect of each structural design parameter on the base shear and roof drift response quantities.

Accuracy of the simple model

In general, excellent agreement is obtained when comparing the trilinear idealized lateral load behavior of the walls obtained using the simple model with the lateral load behavior obtained using the fiber model. Figure 5 shows that for all the walls considered in the study, the decompression point for the simple model matches the decompression point for the fiber model almost exactly. In addition, the figure shows that for all the walls considered in the study, the effective linear limit point for the simple model is generally in agreement with the effective linear limit point for the fiber model. Moreover, the effective linear limit point for the simple model is located in the region where the initial lateral stiffness of the walls begins to reduce significantly. Furthermore, the figure shows that for all the walls considered in the study, the point corresponding to yielding of the post-tensioning steel using the simple model is in good agreement with the occurrence of first yielding in the post-tensioning steel obtained using the fiber model. Last, the point corresponding to confined concrete crushing based on the simple model is in good agreement with the confined concrete crushing point based on the fiber model.

Therefore, it is concluded that the simple model based on closed-form expressions previously derived by Perez et al.[15] defines a trilinear idealized base-shear-roof-drift behavior for unbonded post-tensioned precast concrete walls that accurately represents the lateral-load response obtained using nonlinear fiber model (fiber model) analysis of these walls.

Effect of area of post-tensioning steel

Figure 6 plots the effect of varying the total area of post-tensioning steel in a wall A_p on the base shear and roof drift response quantities. The area A_p was varied while keeping the initial stress in the post-tensioning steel f_{pi} constant. As a result, the initial post-tensioning force P_i and the initial stress in the concrete f_{ci} both increased with an increase in A_p.

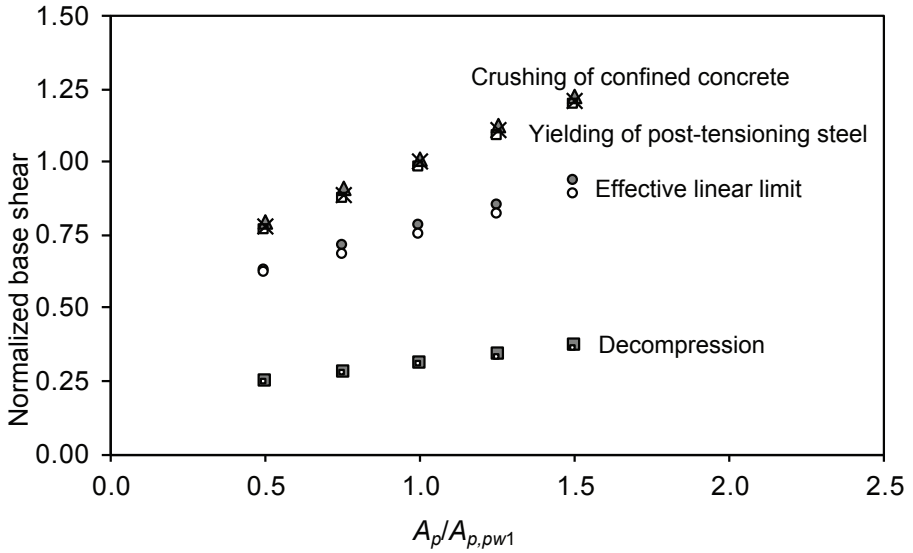

Effect on the wall base shear response quantities

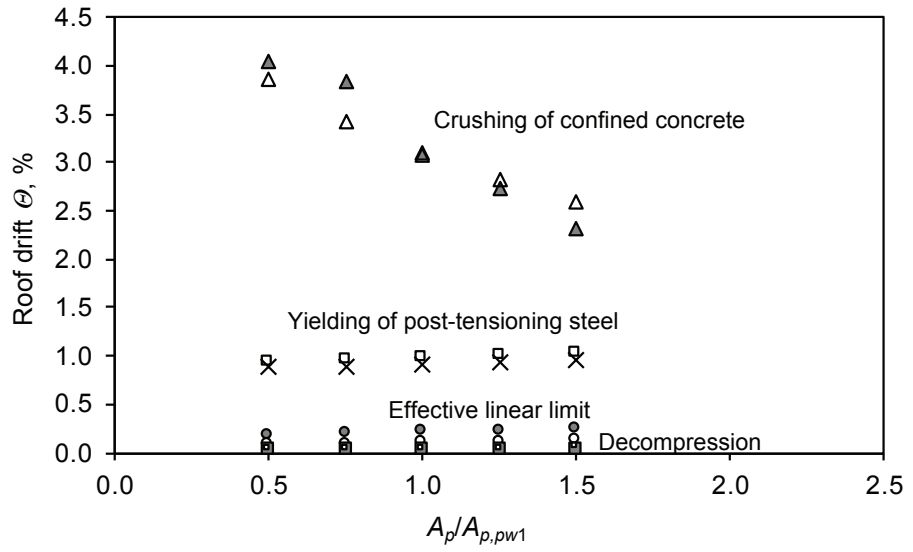

Effect on the wall roof drift response quantities

Figure 6. Effect of area of post-tensioning steel A_p on the wall base shear and roof drift response quantities for walls PW1 and W2 to W5. Note: symbols shown shaded in white represent simple model results, while all other symbols represent fiber model results. Note: $A_{p,pw1}$ = total area of post-tensioning steel in the prototype wall PW1.

Figure 6 shows that as A_p increases, the base shear at decompression V_{dec}, estimated using the simple model and the fiber model, also increases. This occurs because as A_p increases, P_i increases, resulting in a larger clamping force at the wall base and requiring a larger lateral load to cause the wall to decompress. Figure 6 shows that the roof drift at decompression Θ_{dec} increases slightly with A_p for both the simple model and the fiber model. The base shear corresponding to the effective linear limit V_{ell}, estimated using the simple model and the fiber model, significantly increases with increasing A_p. However, the roof drift corresponding to the effective linear limit Θ_{ell} is not significantly affected by A_p in either analytical model.

Figure 6 shows that increasing A_p significantly increases the base shear corresponding to yielding of the post-tensioning steel V_{llp} for both the simple model and the fiber model. However, the roof drift corresponding to yielding of the post-tensioning steel Θ_{llp} is not significantly affected by A_p in either analytical model.

The base shear corresponding to confined concrete crushing V_{ccc} significantly increases with increasing A_p for both the simple model and the fiber model (Fig. 6). However, the roof drift at the confined concrete crushing limit state Θ_{ccc} dramatically decreases with increasing A_p, according to both the sim-

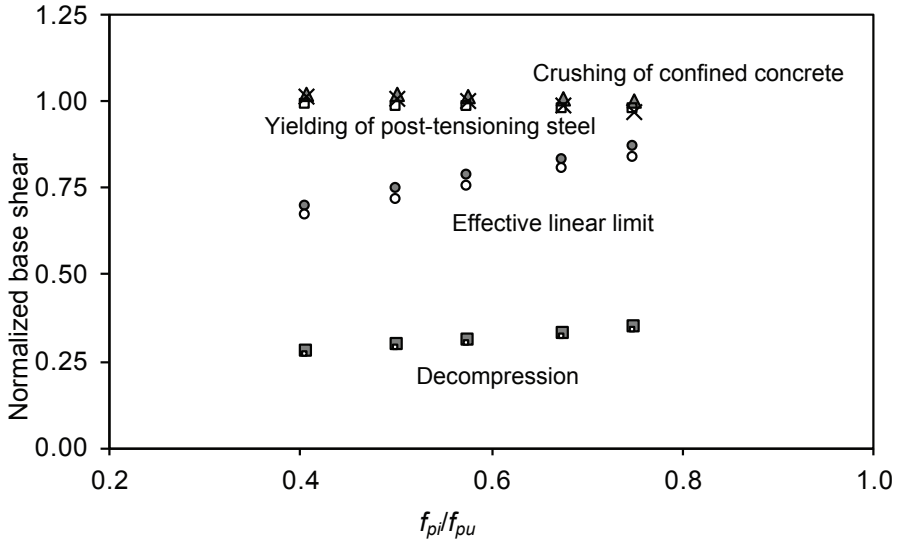

Effect on the wall base shear response quantities

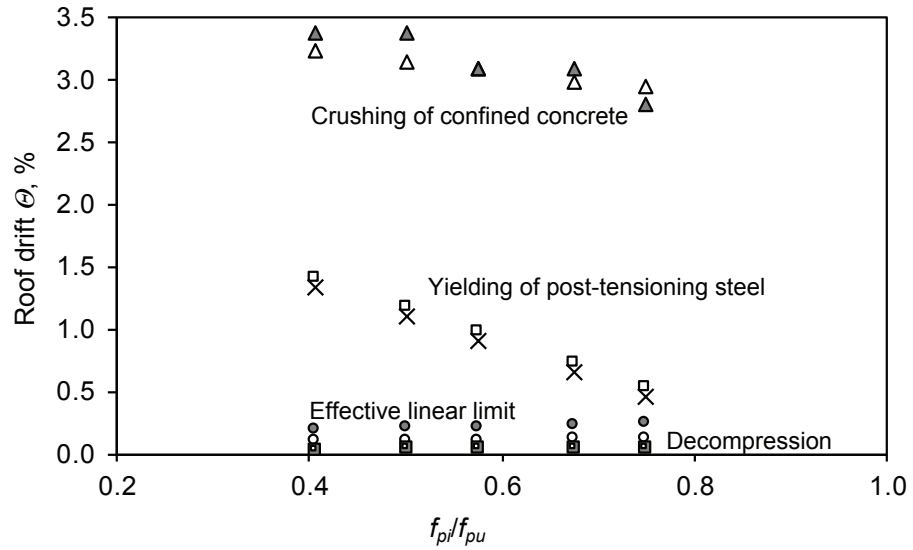

Effect on the wall roof drift response quantities

Figure 7. Effect of initial stress in post-tensioning steel with constant area of post-tensioning steel A_p and variable total initial prestress force P_i on the wall base shear and roof drift response quantities for walls PW1 and W6 to W9. Note: symbols shown shaded in white represent simple model results, while all other symbols represent fiber model results. f_{pi} = stress in post-tensioning steel after the application of prestress forces and gravity loads; f_{pu} = ultimate tensile strength of post-tensioning steel.

ple model and the fiber model. This occurs because increasing A_p while maintaining the f_{pi} constant increases the total force in the post-tensioning steel after gap opening, especially at the limit state of confined concrete crushing. This increase in total post-tensioning steel force requires a larger compression resultant force at the wall base for equilibrium, which, in turn, requires a larger depth of the section in compression at the limit state of confined concrete crushing because the stress capacity of the concrete is limited. With a larger depth of the section in compression, the roof drift is smaller for a given concrete extreme fiber compression strain. Thus, the roof drift at the limit state of confined concrete crushing is reduced when the ultimate confined concrete strain ε_{cu} is reached at the toe of the wall when A_p is increased.

To summarize, the simple model and the fiber model show similar values of base shear and roof drift response, as well as similar trends for the variation of the total area of post-tensioning steel A_p in an unbonded post-tensioned precast concrete wall. Both the simple model and the fiber model show that increasing A_p increases V_{dec}, V_{ell}, V_{llp}, and V_{ccc} and has no significant effect on Θ_{dec}, Θ_{ell}, and Θ_{llp} but significantly reduces Θ_{ccc}.

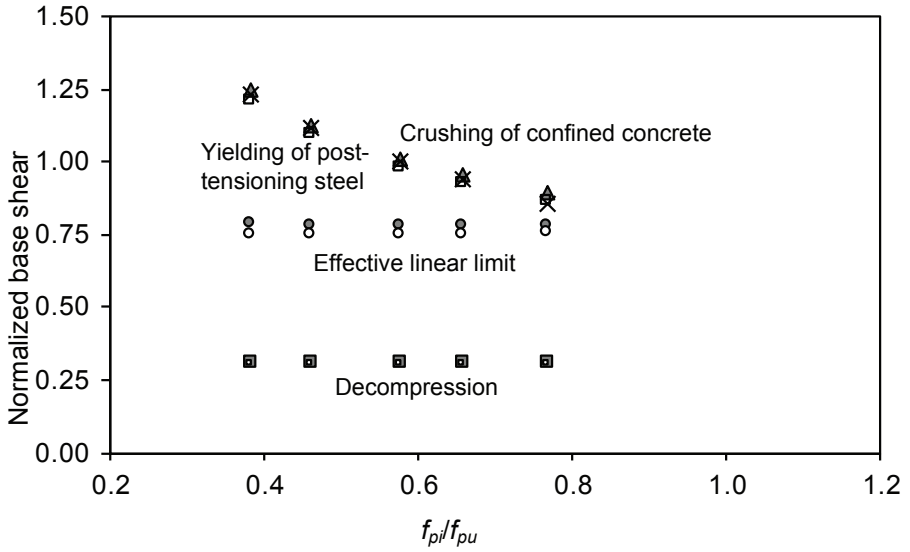

Effect on the wall base shear response quantities

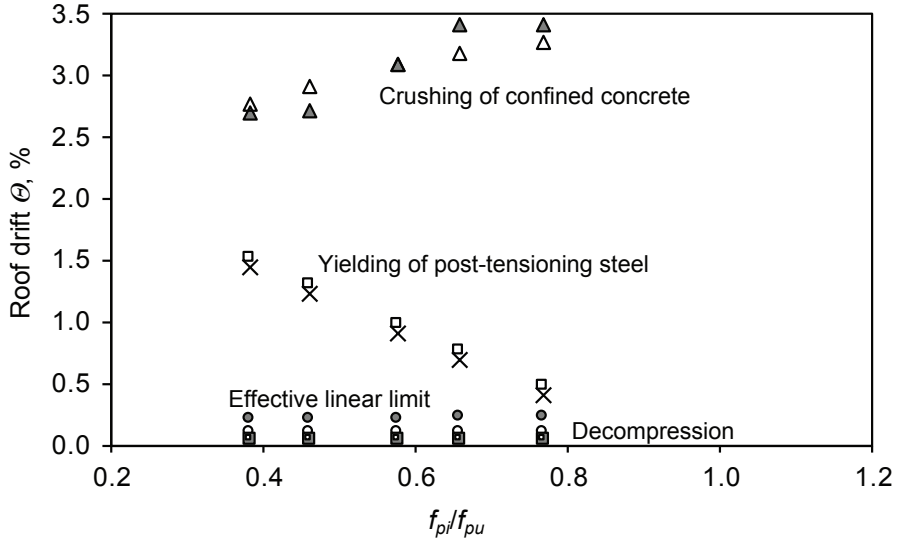

Effect on the wall roof drift response quantities

Figure 8. Effect of initial stress in post-tensioning steel with variable area of post-tensioning steel A_p and constant total initial prestress force P_i on the wall base shear and roof drift response quantities for walls PW1 and W10 to W13. Note: symbols shown shaded in white represent simple model results, while all other symbols represent fiber model results. f_{pi} = stress in post-tensioning steel after the application of prestress forces and gravity loads; f_{pu} = ultimate tensile strength of post-tensioning steel.

Effect of initial stress in post-tensioning steel with constant A_p

Figure 7 plots the effect of varying the initial stress in the post-tensioning steel f_{pi} on the base shear and roof drift response quantities. The area A_p was kept constant so that the total initial post-tensioning force on the wall P_i varied.

Figure 7 shows that as f_{pi} increases, V_{dec} increases for both the simple model and the fiber model. This occurs because increasing the post-tensioning force in a wall increases the clamping force at the wall base, requiring a larger lateral load to cause the wall to decompress. The roof drift at decompression Θ_{dec} is not significantly affected by f_{pi}.

The base shear corresponding to the effective linear limit V_{ell}, estimated using the simple model and the fiber model, increased with increasing f_{pi} (Fig. 7); however, the roof drift corresponding to the effective linear limit Θ_{ell} is not significantly affected by f_{pi} in either analytical model (Fig. 7).

Figure 7 shows that increasing f_{pi} has no significant effect on the base shear corresponding to yielding of the post-tensioning steel V_{llp} for either the simple model or the fiber model.

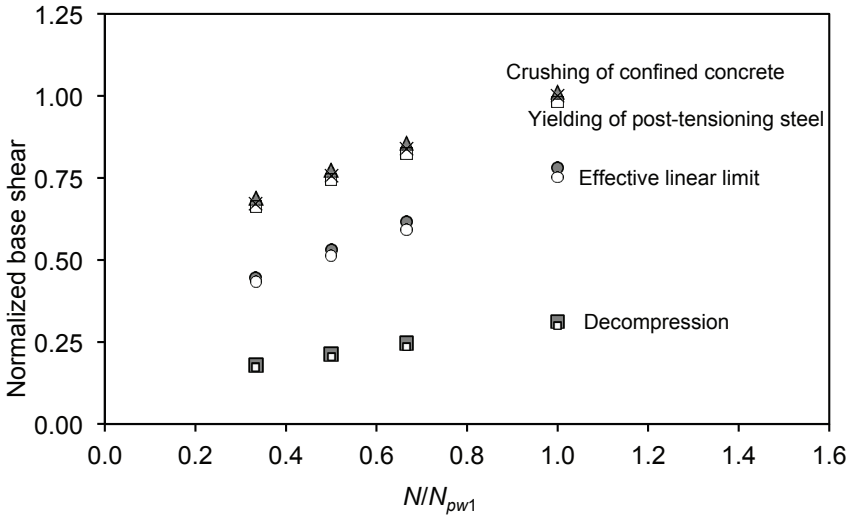

Effect on the wall base shear response quantities

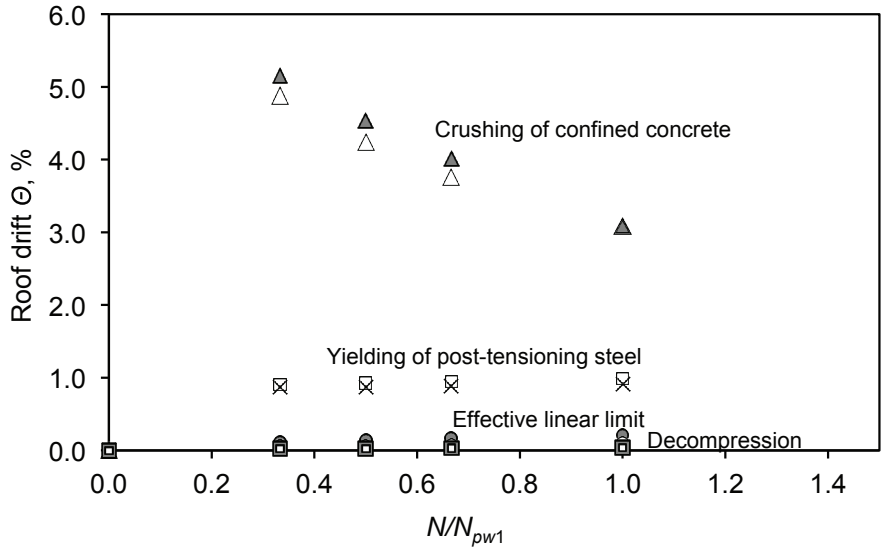

Effect on the wall roof drift response quantities

Figure 9. Effect of initial stress in concrete due to varying gravity loads $f_{ci,N}$ on the wall base shear and roof drift response quantities for walls PW1 and W14 to W16. Note: symbols shown shaded in white represent simple model results, while all other symbols represent fiber model results. f_{pi} = stress in post-tensioning steel after the application of prestress forces and gravity loads; f_{pu} = ultimate tensile strength of post-tensioning steel.

This is because the base shear capacity is influenced mostly by the total area of post-tensioning steel, not f_{pi} (Fig. 6). However, the roof drift corresponding to yielding of the post-tensioning steel Θ_{llp} decreases significantly with increasing f_{pi} for both analytical models (Fig. 7). This occurs because as f_{pi} increases, the initial strain in the post-tensioning steel also increases. Thus, a smaller gap opening along the wall base (and thus a smaller roof drift) is required before the post-tensioning steel yields.

The base shear corresponding to confined concrete crushing V_{ccc} is not significantly affected by f_{pi} for both the simple model and the fiber model (Fig. 7). However, the roof drift at the confined concrete crushing limit state Θ_{ccc} decreases with increasing f_{pi}, according to both the simple model and the fiber model (Fig. 7). This occurs because increasing f_{pi} while maintaining a constant A_p increases f_{ci}. Thus, a smaller gap opening along the wall base (and thus a smaller roof drift) is required before the ultimate confined concrete strain ε_{cu} is reached at the toe of the wall, at which point crushing of confined concrete occurs.

In summary, the simple model and the fiber model show similar values of base shear and roof drift response quantities and

they show similar trends for the variation of the initial stress in the post-tensioning steel f_{pi} with constant A_p and variable P_i. Both analytical models show that increasing f_{pi} with a constant A_p and variable P_i increases V_{dec} and V_{ell}, decreases Θ_{llp} and Θ_{ccc}, and has no significant effect on Θ_{dec}, Θ_{ell}, V_{llp}, and V_{ccc}.

Effect of initial stress in post-tensioning steel with variable A_p and constant P_i

Figure 8 plots the effect of varying the initial stress in the post-tensioning steel f_{pi} on the base shear and roof drift response quantities. The area A_p was simultaneously varied with f_{pi} so that the total initial post-tensioning force on the wall P_i remained constant.

Figure 8 shows that for both the simple model and the fiber model, the base shear and roof drift at decompression, V_{dec} and Θ_{dec} respectively, are not significantly affected by f_{pi} when P_i remains constant. The decompression limit state is unaffected because the initial force in the post-tensioning steel remains the same.

For both the simple model and the fiber model, the base shear and roof drift corresponding to the effective linear limit V_{ell} and Θ_{ell}, respectively, are not significantly affected by f_{pi} when P_i remains constant (Fig. 8). Thus, the walls considered in this particular parameter investigation exhibit the same behavior up to the effective linear limit state (walls W10 to W13 in Fig. 5).

Figure 8 shows that for both the simple model and the fiber model, increasing f_{pi} while maintaining P_i constant significantly reduces the base shear corresponding to yielding of the post-tensioning steel V_{llp}. To maintain a constant P_i while increasing f_{pi} requires a reduction in the area of post-tensioning steel A_p. Since the base shear capacity is influenced mostly by A_p, not f_{pi} (Fig. 6), reducing A_p reduces V_{llp}. Furthermore, the roof drift corresponding to yielding of the post-tensioning steel Θ_{llp} decreases significantly for both the simple model and the fiber model with increasing f_{pi} while maintaining P_i constant (Fig. 8). This occurs because as f_{pi} increases, the initial strain in the post-tensioning steel also increases. Thus, a smaller gap opening along the wall base (and thus a smaller roof drift) is required before the post-tensioning steel yields.

Figure 8 shows that for both the simple model and the fiber model, increasing f_{pi} while maintaining P_i constant significantly reduces the base shear corresponding to crushing of the confined concrete V_{ccc}. Again, to maintain a constant P_i while increasing f_{pi} requires a reduction in the area of post-tensioning steel A_p. Since the base shear capacity is influenced mostly by A_p, reducing A_p reduces V_{ccc}. For both the simple model and the fiber model, the roof drift at the confined concrete crushing limit state Θ_{ccc} increases when f_{pi} increases and P_i remains constant (Fig. 8). Increases in f_{pi} are accompanied by corresponding decreases in A_p. Thus, the walls in this parametric investigation have the same initial post-tensioning force at the wall base and, owing to the reduction in A_p, develop a smaller compression resultant (and a smaller maximum compressive strain) at the wall base under lateral loads. As a result, a larger gap opening along the wall base (or a smaller depth of section in compression), and thus a larger roof drift, is required before the ultimate confined concrete strain ε_{cu} is reached at the toe of the wall.

In summary, both the simple model and the fiber model show similar values of base shear and roof drift response, and they show similar trends for the variation of the initial stress in the post-tensioning steel f_{pi} with variable A_p and constant P_i. Both analytical models show that increasing f_{pi} with a variable A_p and a constant P_i reduces V_{llp}, V_{ccc}, and Θ_{llp}; has no significant effect on V_{dec}, V_{ell}, Θ_{dec}, and Θ_{ell}; and increases Θ_{ccc}.

Effect of initial stress in concrete due to varying gravity loads

Figure 9 plots the effect of varying the initial stress in concrete at the wall base due to varying gravity loads $f_{ci,N}$ on the base shear and roof drift response quantities. Because the cross section of the walls remained unchanged, this parametric investigation was achieved by varying the amount of total gravity load sustained by the walls N.

Figure 9 shows that for both the simple model and the fiber model, the base shear at decompression V_{dec} increases for increasing values of gravity load N. This occurs because increasing N results in a larger clamping force at the wall base, requiring a larger lateral load to cause the wall to decompress. Figure 9 shows that the roof drift at decompression Θ_{dec} is not significantly affected by N for both the simple model and the fiber model.

The base shear corresponding to the effective linear limit V_{ell} estimated using the simple model and the fiber model significantly increases with increasing N (Fig. 9). However, Fig. 9 shows that the roof drift corresponding to the effective linear limit Θ_{ell} increases slightly with N for both the simple model and the fiber model.

Figure 9 shows that increasing N significantly increases the base shear corresponding to yielding of the post-tensioning steel V_{llp} for both the simple model and the fiber model. However, the roof drift corresponding to yielding of the post-tensioning steel Θ_{llp} is not significantly affected by N in either analytical model (Fig. 9).

The base shear corresponding to confined concrete crushing V_{ccc} significantly increases with increasing N for both the simple model and the fiber model (Fig. 9). However, the roof drift at the confined concrete crushing limit state Θ_{ccc} dramatically decreases with increasing N, according to both the simple model and the fiber model (Fig. 9). This occurs because increasing N increases the compression resultant at the wall base, which, in turn, requires a larger depth of the section in compression at the limit state of confined concrete crushing because the stress capacity of the concrete is limited. With a larger depth of the

section in compression, the roof drift is smaller for a given concrete extreme fiber compression strain. Thus, the roof drift at the limit state of confined concrete crushing is reduced when the ultimate confined concrete strain ε_{cu} is reached at the toe of the wall when the total gravity load N is increased.

To summarize, the simple model and the fiber model show similar values of base shear and roof drift response and similar trends for the variation of the total gravity load N supported by an unbonded post-tensioned precast concrete wall. Both the simple model and the fiber model show that increasing N increases V_{dec}, V_{ell}, V_{llp}, and V_{ccc} and has no significant effect on Θ_{dec}, Θ_{ell}, and Θ_{llp} but significantly reduces Θ_{ccc}.

Conclusion

Based on the results of this study, the following conclusions can be drawn:

- The simple model, based on closed-form expressions, defines a trilinear idealized base-shear-roof-drift behavior for unbonded post-tensioned precast concrete walls that accurately represents the lateral-load response obtained using nonlinear fiber model analysis.
- A parametric study of 16 walls indicates that the lateral load behavior, characterized by base shear and roof drift values at selected limit states, of an unbonded post-tensioned wall is influenced by the total area of post-tensioning steel in the wall, the initial prestress forces in a wall, and the total gravity load sustained by the wall.
- Both the simple model and the fiber model show similar values of base shear and roof drift response quantities, and they show similar trends for each parameter variation.
- The simple model is recommended for the seismic design of unbonded post-tensioned precast concrete walls.

Acknowledgments

This study was partially funded by the McNair Scholars Program at California State Polytechnic University, Pomona. Yahya Kurama, professor and associate chair in the Department of Civil and Environmental Engineering and Earth Sciences at the University of Notre Dame in Notre Dame, Ind., is acknowledged for providing the authors with the fiber model of the prototype wall used in this study.

References

1. Fintel, M. 1995. "Performance of Buildings with Shear Walls in Earthquakes of the Last Thirty Years." *PCI Journal* 40 (3): 62–80.
2. Cheok, G., W. Stone, and H. Lew. 1993. "Performance of ⅓-Scale Model Precast Concrete Beam–Column Connections Subjected to Cyclic Inelastic Loads—Report No. 3." NISTIR 5246. National Institute of Standards and Technology, Gaithersburg, MD.
3. MacRae, G., and M. Priestley. 1994. "Precast Post-Tensioned Ungrouted Concrete Beam-Column Subassemblage Tests." PRESSS (Precast Seismic Structural Systems) 94/01. Department of Applied Mechanics and Engineering Sciences, Structural Systems, University of California, San Diego, CA.
4. Priestley, M., and J. Tao. 1993. "Seismic Response of Precast Prestressed Concrete Frames with Partially Debonded Tendons." *PCI Journal* 38 (1): 58–69.
5. Perez, F. J., S. Pessiki, and R. Sause. 2013. "Experimental Lateral Load Response of Unbonded Post-Tensioned Precast Concrete Walls." *ACI Structural Journal* 110 (6): 1045–1055.
6. Perez, F. J., S. Pessiki, and R. Sause. 2004. "Experimental and Analytical Lateral Load Response of Unbonded Post-Tensioned Precast Concrete Walls." Report 04-11. ATLSS (Center for Advanced Technology for Large Structural Systems), Lehigh University, Bethlehem, PA.
7. Kurama, Y. C., S. Sritharan, R. B. Fleischman, J. I. Restrepo, R. S. Henry, N. M. Cleland, S. K. Ghosh, and P. Bonelli. 2018. "Seismic-Resistant Precast Concrete Structures: State of the Art." *ASCE Journal of Structural Engineering* 144 (4): 03118001-1–03118001-18.
8. Kurama, Y. C. 2002. "Hybrid Post-Tensioned Precast Concrete Walls for Use in Seismic Regions." *PCI Journal* 47 (5): 36–59.
9. Restrepo, J. I., and A. Rahman. 2007. "Seismic Performance of Self-Centering Structural Walls Incorporating Energy Dissipators." *ASCE Journal of Structural Engineering* 133 (11): 1560–1570.
10. Smith, B. J., Y. C. Kurama, and M. J. McGinnis. 2012. "Hybrid Precast Wall Systems for Seismic Regions." Report NDSE-2012-01. Department of Civil Engineering and Geological Sciences, University of Notre Dame, Notre Dame, IN.
11. Palermo, A., and S. Pampanin. 2008. "Analysis and Simplified Design of Precast Jointed Ductile Connections." The 14th World Conference on Earthquake Engineering, October 12–17, 2008, Beijing, China.
12. Kurama, Y. C., S. Pessiki, R. Sause, L.-W. Lu, and M. El-Sheikh. 1996. "Analytical Modeling and Lateral Load Behavior of Unbonded Post-Tensioned Precast Concrete Walls." Report EQ-96-02. ATLSS, Lehigh University, Bethlehem, PA.
13. Kurama, Y. C., R. Sause, S. Pessiki, and L.-W. Lu. 1999.

"Lateral Load Behavior and Seismic Design of Unbonded Post-Tensioned Precast Concrete Walls." *ACI Structural Journal* 96 (4): 622–632.

14. Prakash, V., and G. Powell. 1993. "DRAIN-2DX Base Program Description and User Guide; Version 1.10." Report UCB/SEMM-93/17. Structural Engineering Mechanics and Materials, Department of Civil Engineering, University of California, Berkeley, CA.

15. Perez, F. J., R. Sause, and S. Pessiki. 2007. "Analytical and Experimental Lateral Load Behavior of Unbonded Post-Tensioned Precast Concrete Walls." *ASCE Journal of Structural Engineering* 133 (11). https://doi.org/10.1061/(ASCE)0733-9445(2007)133:11(1531).

16. Kurama, Y. C., S. Pessiki, R. Sause, and L.-W. Lu. 1999. "Seismic Behavior and Design of Unbonded Post-Tensioned Precast Concrete Walls." *PCI Journal* 44 (3): 72–89.

17. Mander, J., M. Priestley, and R. Park. 1988. "Theoretical Stress-Strain Model for Confined Concrete." *Journal of Structural Engineering, American Society of Civil Engineers* 114 (8): 1804–1826.

Notation

A_p = total area of post-tensioning steel in the wall

A_{p1} = total area of post-tensioning steel in post-tensioning steel group 1

A_{p2} = total area of post-tensioning steel in post-tensioning steel group 2

A_{p3} = total area of post-tensioning steel in post-tensioning steel group 3

$A_{p,pw1}$ = total area of post-tensioning steel in the prototype wall PW1

A'_w = effective shear area of the wall

$A_{w,net}$ = net cross-sectional area of the wall

c = contact length at wall base

C = concrete compression stress resultant at wall base

e_{Ni} = eccentricity of N_i measured from the wall centerline

e_{Nr} = eccentricity of N_r measured from the wall centerline

e_p = eccentricity of post-tensioning steel from wall centerline to centroid of post-tensioning steel group

E_c = elastic modulus of concrete

E_p = modulus of elasticity of post-tensioning steel

f'_c = unconfined concrete compressive strength

f'_{cc} = confined concrete compressive strength

f_{ci} = initial stress in concrete due to post-tensioning and gravity loads

$f_{ci,N}$ = initial stress in concrete due to gravity loads

$f_{ci,P}$ = average initial stress in concrete due to prestressing

f_{p1i} = initial stress in post-tensioning steel group 1

f_{p2i} = initial stress in post-tensioning steel group 2

f_{p3i} = initial stress in post-tensioning steel group 3

f_{pi} = stress in post-tensioning steel after the application of prestress forces and gravity loads (also referred to as the initial stress in the post-tensioning steel)

f_{pu} = ultimate tensile strength of post-tensioning steel

f_{py} = yield stress of post-tensioning steel

$F_{w,i}$ = lateral force on wall at floor i

$F_{w,r}$ = lateral force on wall at roof level

G_c = shear modulus of concrete

h_{cr} = height over which confining reinforcement is provided from the wall base

H_{cr} = critical confined concrete crushing height measured from the wall base

H_i = height of floor level i measured from the base of the wall

H_r = height of roof level measured from the base of the wall = H_w

H_w = total wall height

i = floor level

I_w = moment of inertia of the uncracked section of the wall

l_{cr} = length over which confining reinforcement is provided from each end of the wall

l_w = wall length

N = total gravity load at the wall base

N_i = gravity load at *i*th floor level, including panel self-weight

N_{pw1} = total gravity load at the base of prototype wall PW1

N_r = gravity load at roof level, excluding top panel self-weight

P_i = total force in the post-tensioning steel after the application of prestress forces and gravity loads (also referred to as the total initial prestress force on the wall)

r = total number of stories in a wall

r_{F1} = ratio of the force in the 1st floor level to the wall base shear

r_{F2} = ratio of the force in the 2nd floor level to the wall base shear

r_{F3} = ratio of the force in the 3rd floor level to the wall base shear

r_{F4} = ratio of the force in the 4th floor level to the wall base shear

r_{F5} = ratio of the force in the 5th floor level to the wall base shear

r_{Fi} = ratio of the force in the *i*th floor level to the wall base shear

r_{Fr} = ratio of the force at the roof level to the wall base shear

r_{Hi} = ratio of the *i*th floor height to the total height of the wall

r_{H1} = ratio of the 1st floor level height to the total height of the wall

r_{H2} = ratio of the 2nd floor level height to the total height of the wall

r_{H3} = ratio of the 3rd floor level height to the total height of the wall

r_{H4} = ratio of the 4th floor level height to the total height of the wall

r_{H5} = ratio of the 5th floor level height to the total height of the wall

r_{Hr} = ratio of the roof height to the total height of the wall (equal to unity)

t_w = wall thickness

t''_w = wall thickness measured between centerlines of confining reinforcement

T_1 = total force in post-tensioning steel group 1

T_{1i} = total initial prestress force in post-tensioning steel group 1

T_2 = total force in post-tensioning steel group 2

T_{2i} = total initial prestress force in post-tensioning steel group 2

T_3 = total force in post-tensioning steel group 3

T_{3i} = total initial prestress force in post-tensioning steel group 3

V = base shear

V_{ccc} = base shear at limit state corresponding to crushing of confined concrete

V_{dec} = base shear at limit state corresponding to decompression at the wall base

V_{ell} = base shear at limit state corresponding to the effective linear limit

V_{llp} = base shear at limit state corresponding to yielding of post-tensioning steel

V_w = wall base shear (equal to sum of applied lateral loads)

ε_{cu} = ultimate strain capacity of confined concrete

ρ_{sp} = volumetric ratio of spiral reinforcement

Θ = roof drift

Θ_{ccc} = roof drift at limit state corresponding to crushing of confined concrete

Θ_{dec} = roof drift at limit state corresponding to decompression at the wall base

Θ_{ell} = roof drift at limit state corresponding to the effective linear limit

Θ_{llp} = roof drift at limit state corresponding to yielding of post-tensioning steel

About the authors

Felipe J. Perez, PhD, PE, is an associate professor in the Civil Engineering Department at California State Polytechnic University, Pomona.

Omar Mauricio, PE, is a master's degree student in the Civil Engineering Department at California State Polytechnic University, Pomona.

Abstract

Previous research on unbonded post-tensioned precast concrete walls included the development of a nonlinear wall model based on fiber elements and of a design-oriented simple analytical model based on generalized closed-form expressions that define a trilinear idealized wall response under combined gravity and lateral loads. Each model considers several key limit states in the lateral-load response of unbonded post-tensioned precast concrete walls. The fiber model and simple model were previously validated using limited available experimental results on unbonded post-tensioned precast concrete walls. This paper presents the results of a parametric study conducted using the fiber model and the simple model to investigate the adequacy of the simple model for a broader range of parameters. Results show that the simple model accurately represents the lateral-load response obtained using the fiber model. Furthermore, the simple model and the fiber model show similar values of base shear and roof drift response, and they show similar trends for each parameter variation. Thus, the simple model is recommended for the seismic design of unbonded post-tensioned precast concrete walls.

Keywords

Analytical, model, post-tensioned, precast seismic structural system, unbonded, wall.

Review policy

This paper was reviewed in accordance with the Precast/Prestressed Concrete Institute's peer-review process.

Reader comments

Please address any reader comments to *PCI Journal* editor-in-chief Emily Lorenz at elorenz@pci.org or Precast/Prestressed Concrete Institute, c/o *PCI Journal*, 200 W. Adams St., Suite 2100, Chicago, IL 60606.